Why Pt Survives but Pd Suffers From SO$_x$ Poisoning?

Hom N. Sharma,[†,§] Vinit Sharma,[‡] Ashish B. Mhadeshwar,[§,†] and Rampi Ramprasad*[,‡]

[†]Chemical and Biomolecular Engineering Department, University of Connecticut, Storrs, Connecticut 06269, United States
[‡]Material Science and Engineering Department, University of Connecticut, Storrs, Connecticut 06269, United States
[§]Center for Clean Energy Engineering, University of Connecticut, Storrs, Connecticut 06269, United States

Ⓢ *Supporting Information*

ABSTRACT: Pd is more prone to sulfation compared to Pt. Given the chemical similarity between Pt and Pd, the radical divide in their tendencies for sulfation remains a puzzle. We explain this intriguing difference using an extensive first-principles thermodynamics analysis and computed bulk and surface phase diagrams. In practically relevant temperatures and O$_2$ and SO$_3$ partial pressures, we find that Pt and Pd show significantly different tendencies for oxidation and sulfation. PdO formation is favored even at low oxygen chemical potential; however, PtO$_2$ formation is not favorable in catalytically relevant conditions. Similarly, PdSO$_4$, and adsorbed SO$_3$ and oxygen species on clean and oxidized surfaces are highly favored, whereas PtSO$_4$ formation does not occur at typical temperature and pressure conditions. Finally, several descriptors are identified that correlate to heightened sulfation tendencies, such as the critical O chemical potential for bulk oxide and surface oxide formation, chemical potentials O and SO$_3$ for bulk sulfate formation, and SO$_3$ binding strength on metal surface-oxide layers, which can be used to explore promising sulfur resistant catalysts.
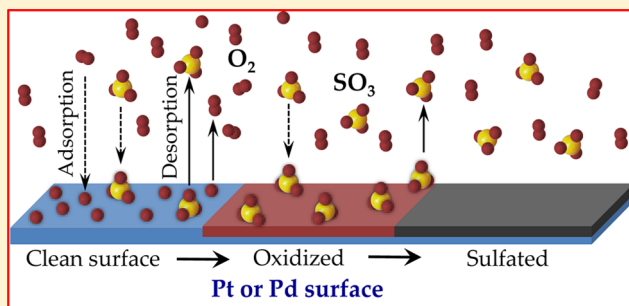
Oxides of sulfur, predominantly SO$_3$ generated from the oxidation of SO$_2$, poison the noble metal based emissions aftertreatment catalysts such as the diesel oxidation catalysts (DOCs) by altering metal surface properties, blocking other emissions species/adsorbates, changing the reaction selectivity, and forming stable metal sulfates.[1−8] Traditionally, Pt-based oxidation catalysts have been the most preferred option for the oxidation of diesel engine emissions due to their superior capability to resist sulfation (i.e., formation of PtSO$_4$ or other sulfates).[10−12] However, the high cost of Pt and its tendency to sinter at the high operating temperatures encountered have forced the inclusion of Pd in the currently used state-of-the-art oxidation catalysts.[6,7] Although Pd by itself is a good oxidation catalyst, has low cost, and resists sintering (unlike Pt), it suffers from sulfur poisoning.[6−9] Indeed, many experimental and computational studies[1−3,8,10−12] directly point to the heightened tendency for Pd sulfation—especially, formation of PdSO$_4$. On the other hand, no evidence exists for the formation of PtSO$_4$ even under highly oxidizing and sulfating conditions. Given the chemical similarity between Pt and Pd, the radical divide in their tendencies for sulfation remains a puzzle. A clear understanding of the circumstances (environment, chemical attributes, descriptors, etc.) that contribute to the different sulfation tendencies of Pt and Pd will guide us in rationally designing potentially lower-cost, higher-performance sulfur-resistant catalysts.

This work aims to provide fundamental insights pertaining to the intrinsic tendency (or lack thereof) of Pt and Pd to undergo sulfation via a comprehensive first-principles thermodynamics

study. The thermodynamic analysis has resulted in accurate and feature-rich bulk and surface phase diagrams of Pt and Pd when exposed to reservoirs of O$_2$ and SO$_3$. This has also aided in the identification of descriptors or key features that make Pt different from Pd. Owing to the complex nature of the sulfation process, capturing a large spectrum of possible bulk and surface phases as a function of the environmental conditions is critical. Figure 1 collects the anticipated and known stable phases when Pt or Pd is exposed to oxidizing or sulfating conditions (i.e., O$_2$ and SO$_3$ environments). This collage of possible phases includes pure bulk metals, bulk oxides, and bulk sulfates as well as surface metallic forms, surfaces partially or wholly covered with O or SO$_3$ or both, surface oxides, and surface sulfates. When prior experimental or computational information was available for a particular phase, it was used in our calculations. However, when such information was not available (e.g., in the case of PtSO$_4$), we determined the atomic level structure using a structure search algorithm in the Universal Structure Predictor: Evolutionary Xtallography (USPEX) method.[13,14]

Once the catalog of possible phases was assembled, the Gibbs free energy of formation of each of the phases with respect to the appropriate reference states was computed using the density functional theory (DFT) total energies, DFT
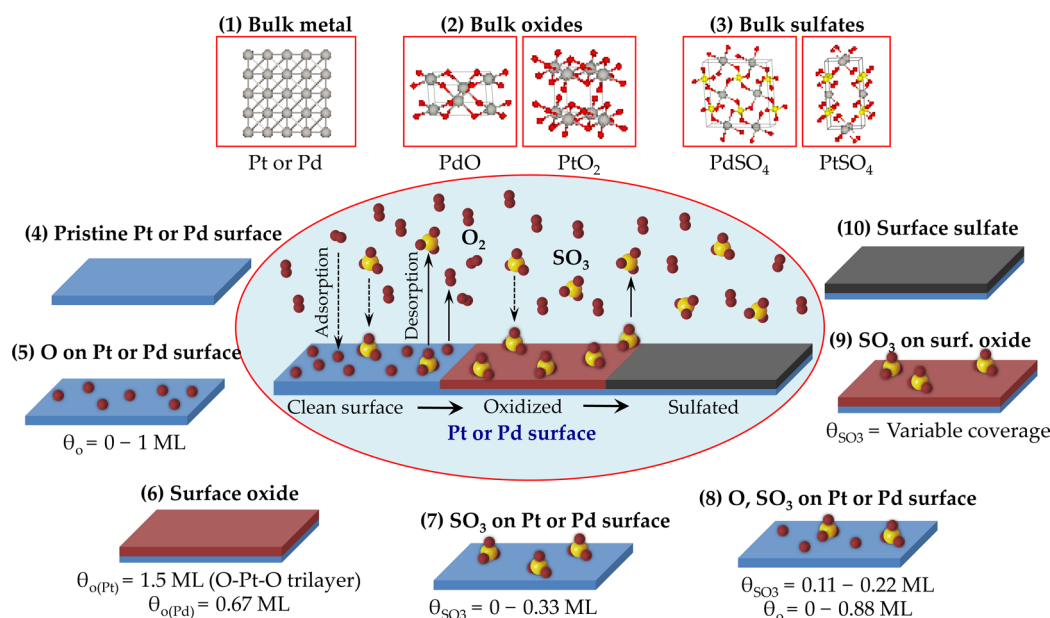
Figure 1. Schematics of the representative stable structures of various bulk and surface phases in the thermodynamic equilibrium containing O_2 and SO_3 for the temperature and pressure range considered in this study. The middle region (inside the circular boundary) represents a catalyst surface exposed to wide ranges of temperature and pressure conditions, where gas phase O_2 and SO_3 along with adsorbed O and SO_3 on Pt or Pd surface are also shown. Panels 1−3 at the top represent the bulk phases (i.e., bulk metal, metal oxides, and bulk sulfates), and panels 4−10 represent various possible surface phases of Pt and Pd (i.e., pristine surfaces, O or SO_3 on the metal surfaces, surface oxides, SO_3 on the surface oxides, and surface sulfates) in an anticlockwise order to the ultimate sulfate phase. The blue, brown, and black colors represent the clean metal surface, surface oxide, and the surface sulfate layer, respectively. Similarly, the silver, red, and yellow spheres represent the Pt or Pd, oxygen, and sulfur, respectively.

phonon density of states, and the statistical mechanics of ideal diatomic (O_2) and polyatomic (SO_3) gases. The Gibbs free energy inherently contains temperature and pressure dependence. Although the pressure dependence comes entirely through the chemical potentials of the gas phase species (μ_{O_2} and μ_{SO_3} of O_2 and SO_3, respectively), the temperature dependence arises due to the gas phase species as well as due to the vibrational degrees of freedom of the condensed phases. The latter is generally ignored due to the severe computational expense of phonon computations, but it is computed and shown to have no significant impact on outcome of the present work. Hence, the contribution is not included in the phase diagrams shown in this paper. Furthermore, this formulation neglects the configurational entropic contributions because it was found in the past to have no significant impact on the results, especially features of the phase diagrams.[15] The free energies were then used to construct bulk and surface phase diagrams, revealing clear differences between Pt and Pd insofar as their thermodynamic tendencies for both oxidation and sulfation are concerned. Details of the DFT calculations are described later in Computational Methods section. Vibrational modes computations and surface free energy computations are given in the Supporting Information.

A simple yet effective starting point is to consider the bulk phases (metal, oxide and sulfate) shown in panels 1−3 of Figure 1. Both Pt and Pd metals are *fcc* structures (space group 225, $Fm\overline{3}m$) with very similar lattice parameters. However, the experimentally known most stable bulk oxides of Pt and Pd are quite different from each other.[16] A dioxide compound PtO_2 (space group 164, $P\overline{3}m1$) is the most stable oxide of Pt, whereas a monoxide compound PdO (space group 131, $P4_2/mmc$) is the only known stable oxide of Pd. In the case of metal sulfates, $PdSO_4$ (space group 15, $C2/c$) is well known

experimentally; however, no information is available about $PtSO_4$ to the best of our knowledge. Therefore, we have used the USPEX method[13,14] and have identified a tetragonal $PtSO_4$ phase (space group 84, $P4_2/m$).[17] The dynamical stability of this phase was confirmed via a phonon band structure calculation, which revealed no modes with imaginary frequencies. In order to validate the veracity of the USPEX method for this class of systems, the structure of $PdSO_4$ was also predicted using USPEX. It is reassuring to note that the correct experimentally known ground state structure of $PdSO_4$ is indeed recovered. Details concerning the structure prediction results, as well as the predicted geometries of the selected phases along with comparisons to past experimental and computation work are provided in the Supporting Information.

The free energies of the bulk metals, oxides, and sulfates were then used to compute the phase diagrams for both Pt and Pd, which are shown in Figure 2. As noted earlier, the free energy depends on the temperature and the O_2 and SO_3 partial pressures. Essentially, this figure shows the most stable phase (i.e., the one with the lowest free energy) for a given choice of the temperature and pressure dependent parts of the O_2 and SO_3 chemical potentials (represented using $\Delta\mu_{O_2}$ and $\Delta\mu_{SO_3}$). For convenience, the O_2 and SO_3 partial pressure ranges for two choices of temperatures (300 and 700 K) are also shown. It is evident that PdO formation is more favored than PtO_2 formation as the onset of the PdO phase region occurs at less oxidizing conditions ($\Delta\mu_{O_2} = -1.88$ eV) compared to PtO_2 ($\Delta\mu_{O_2} = -1.42$ eV). More importantly, the $PdSO_4$ phase region is a lot more prominent than the $PtSO_4$ phase region for the same range of chemical potentials or temperature−pressure ranges. In fact, the stability range of $PtSO_4$ lies outside of normal pressure conditions at ambient (300 K) or higher temperatures. This may explain why there is no experimental
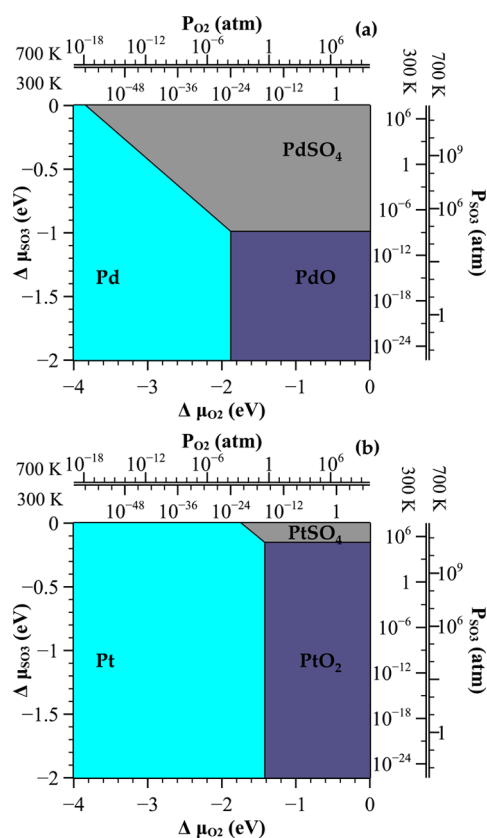
Figure 2. Bulk phase diagrams showing metal, metal oxide, and metal sulfate (structures are shown in Figure 1) in the given ranges of $\Delta\mu_{SO_3}$ and $\Delta\mu_{O_2}$. (a) Bulk phase diagram with Pd, PdO, and PdSO$_4$ and (b) bulk phase diagram with Pt, PtO$_2$, and PtSO$_4$. Chemical potential ranges are translated into a pressure range for two representative temperatures (300 and 700 K). The stability regions of bulk sulfates show the most prominent differences.

information available for PtSO$_4$ thus far.[15] The clear thermodynamic resistance for PtSO$_4$ formation (compared to PdSO$_4$) in the bulk form is indicative of Pt's resistance to sulfur poisoning and could be used as a screening criterion to identify potentially sulfur resistant catalysts.

Although bulk thermodynamics provides a good starting point, catalytically more realistic conditions involve surface phenomena. Therefore, we investigated the possible surface phases on both metal surfaces in oxidizing and sulfating environments. In panels 4−6 of Figure 1, we show the stable surface phases while increasing the oxygen partial pressure. Results (discussed later in more details) show greater affinity of Pd surface toward oxygen with highly favored surface oxide formation. Similarly, we show the stable phases of SO$_3$ on clean surface and coadsorbed oxygen and SO$_3$ in panels 7 and 8, respectively. Panel 9 shows a more interesting phase of SO$_3$ on the oxidized surfaces of Pt and Pd. We observed that the affinity of SO$_3$ is significant on PdO only. Further interaction of SO$_3$ and the surface oxide could potentially result in a surface sulfate as shown in panel 10, and ultimately in the bulk sulfate in panel 3. These phases are discussed next, resulting in the surface phase diagrams for Pt and Pd surfaces when exposed to O$_2$ and SO$_3$.

Due to significantly high oxygen concentration (∼10%) in realistic exhaust conditions,[6,7] a natural step here is to investigate the oxygen interactions on the surfaces. Exper-

imentally observed stable phases of O on Pt(111) and Pd(111) due to O$_2$ exposure involve $p(2 \times 2)$ and $c(2 \times 2)$ configurations with possibility of higher coverage ($\theta_O \sim 1$ ML) when the Pt(111) surface is exposed to NO$_2$ or O$_3$.[18,19] Hence, we investigated the entire range (0−1 ML) of O coverage on both surfaces (higher O coverage is possible in surface oxides, as discussed in the next paragraph). By considering a variety of configurational possibilities (as described in the Supporting Information), this approach allowed us to fully capture lateral or adsorbate−adsorbate interactions. In general, we observed very similar oxygen interaction behavior (binding strength and lateral interaction patterns) on both Pt(111) and Pd(111) surfaces. Binding energies of oxygen on both metal surfaces are given in Supporting Information.

An elevated oxygen concentration on the metal surface can proceed to a partially oxidized phase (i.e., the surface oxide phases shown in panel 6 of Figure 1). The surface oxide models for Pt(111) and Pd(111) surfaces considered here are guided by HRCLS, STM, LEED, and XRD experimental observations.[20−22] Experimental and computational results suggest that the surface oxide layer formation on Pt(111) and Pd(111) surfaces results in different types of arrangements of metal and oxygen atoms.[23−25] A (O−Pt−O) trilayer structure of Pt surface oxide on a (2×2) surface contains only three Pt atoms (unlike four Pt atoms on a clean surface) and six O atoms. LEED patterns show α-PtO$_2$(0001) (2×2) overlayers on the Pt(111) surface.[20] On the other hand, a distinct Pd$_5$O$_4$ type (with repetitive structure pattern of five Pd and four O) stable surface oxide layer on Pd(111) was represented by $7 \times$ (Pd$_5$O$_4$) model. This unique structure corresponds to a 0.67 ML oxygen coverage; it has two types of Pd atoms which are either 2- or 4-fold coordinated to O atoms and two types of O atoms that are either 3-fold (bonded to in-plane Pd atoms) or 4-fold (bonded to in-plane and subsurface Pd atoms) coordinated to Pd atoms. The LEED pattern shows that the structure is commensurate in the $[2\ \bar{1}\ \bar{1}]$ direction.[26] We note the existence of possible subsurface oxygen configurations on both metals. Todorova et al. showed that subsurface oxygen on transition metals is initially always less stable than on-surface oxygen adsorption. However, with increasing coverage this preference vanishes, and oxygen incorporation becomes more favorable above coverages of ∼0.5 ML.[27,28] We considered the most stable/favored subsurface site tetra-I[29] (i.e., the site directly below the 3-fold hcp position on (111) surface) to compute the energetics of the on-surface and subsurface oxygen adsorption. Our results show that on-surface (fcc)/subsurface (tetra-I) configuration favors only after on-surface fcc coverage of 0.5 ML on Pd(111), whereas it favors only above the on-surface fcc coverage of 0.75 ML on Pt(111) (in Figure 3). The subsurface only oxygen adsorption ($\theta_o = 0.25$ ML) at tetra-I site was highly endothermic for both Pt(111) and Pd(111). However, the subsurface/on-surface combination becomes exothermic on/above $\theta_o = 0.5$ ML. This observation clearly shows the favorability of the on-surface oxygen adsorption at the lower coverage. In general, the adsorption of oxygen on the metal surface is followed by the on-surface/subsurface oxygen configurations, which finally transforms to the fully oxidized metal oxide layers. While evaluating the stability based on thermodynamics, we observed that the surface oxides phases are thermodynamically more stable than any subsurface oxygen configurations and even the experimentally known $c(2 \times 2)$-O (0.5 ML) configuration.[30] Thus, they do not appear on the
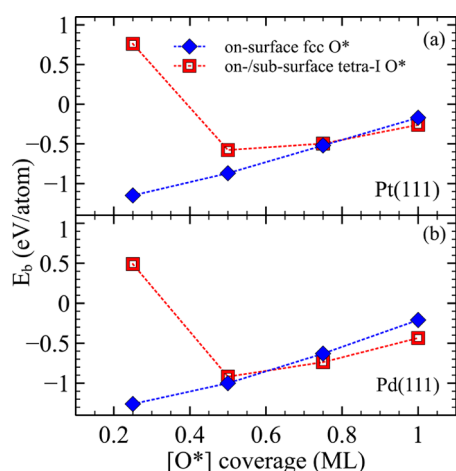
Figure 3. DFT computed average binding energy E_b as a function of total O* coverage with on-surface *fcc* and subsurface tetra-I sites of Pt(111) and Pd(111) shown in panels a and b, respectively. The blue symbols represent the binding energies of oxygen for on-surface *fcc* sites of (111) surface. The red symbols represent the binding energies of oxygen for *fcc*/tetra-I combinations. A (2 × 2) surface supercell was used for the computations. The red symbol at θ_o = 0.25 ML represents the oxygen on subsurface tetra-I site only and higher coverages (>θ_o = 0.25 ML) represent the combination of O* with one oxygen in subsurface tetra-I and rest of oxygen on surface *fcc* sites. Dotted lines are drawn to guide the eyes. On-surface *fcc* O* coverage below 0.5 ML is always stable on both surfaces.

phase diagrams constructed based on thermodynamics. Utilizing the information from oxygen adsorption and surface oxides formation, we created detailed phase diagram of oxygen on both (Pd (111) and Pt(111)) surfaces. Our calculated phase boundaries for various phases of oxygen adsorption on both surfaces are in good agreement with known experimental results.[31−36] Details of the on-surface/subsurface oxygen adsorption and phase diagrams are shown in Supporting Information (Table S3, Figure S3).

Another spectrum of stable phases may arise due to the presence of SO₃ on the surface (panel 7 of Figure 1). SO₃ shows a strong affinity toward both surfaces, albeit slightly stronger on Pt(111) as shown by the binding energy numbers in Figure 4. An upright standing chair-shaped configuration on *fcc* sites is the preferred one in both cases.[6,37] Given the bulky nature of the SO₃ molecule, the maximum coverage on the (111) surface could only reach up to 0.33 ML in a (3 × 3) surface supercell. Size of the molecule is responsible for the significant lateral interactions between adjacent SO₃ molecules (note the sharp decrease of SO₃ binding energy with coverage in Figure 4). We note that the configurational space can be large for a higher coverage; however, the overall outcome due to the selection of our surface models will not change. Four representative stable configurations corresponding to a coverage range of 0.06 to 0.33 ML are considered for the generation of phase diagrams (panels 7a−d of Figure 5). Computed binding energies and the phase diagrams of SO₃ adsorption in Pt(111) and Pd(111) surfaces are given in the Supporting Information (Table S4 and Figure S4).

A more interesting condition involves the coadsorbed environment of SO₃ and oxygen on the metal surfaces as shown in panels 8a−c of Figure 5. In a (3 × 3) surface supercell, we investigated two SO₃ coverages (i.e., θ_{SO_3} = 0.11 ML and θ_{SO_3} = 0.22 ML) and possible O coverages (i.e., up to
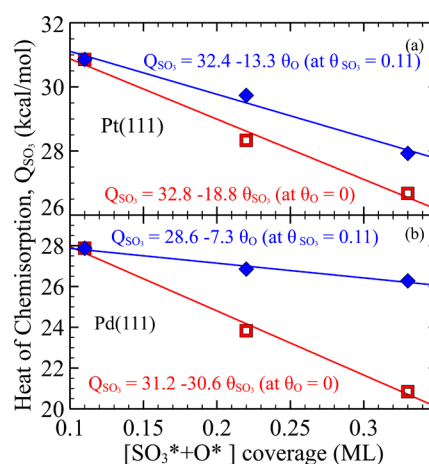
Figure 4. DFT computed heat of chemisorption of SO₃ versus SO₃* and SO₃* + O* coverages on Pt(111) and Pd(111) surfaces shown in panels a and b, respectively. The red lines represent a linear fit to SO₃*−SO₃* interactions. The blue lines represent a linear fit for the SO₃*−O* interactions as a function of O* coverage at a fixed θ_{SO_3} = 0.11 ML. A (3 × 3) surface supercell was used for the energy computations. For the cross-interactions calculations, a fixed surface coverage of SO₃ (at θ_{SO_3} = 0.11 ML) was used while varying the O* coverage.

0.89 ML). For the condition with one SO₃ molecule (i.e., θ_{SO_3} = 0.11 ML) on the surface, the maximum stable oxygen coverage was 0.33 ML, whereas the maximum coverage of O decreased to 0.22 ML with two SO₃ molecules (i.e., θ_{SO_3} = 0.22 ML) on the surface. Further addition of O on the surface caused destabilization and desorption of the SO₃ molecule from the surface. This is due to the larger binding strength of O on metal (Pt and Pd) surfaces and also due to lateral adsorbate−adsorbate interactions between O and SO₃ as shown in Figure 4. It shows the change in binding energies of SO₃ due to oxygen addition on the Pt(111) and Pd(111) surfaces. Computational details of the coadsorption and the SO₃*−O* cross interactions are given in the Supporting Information.

With no experimental or computational information on the interactions of O and SO₃ on the oxidized surfaces, it remains an unfamiliar and unexplored territory. This study examined the possible interactions of O and SO₃ on the surface oxides of both Pt and Pd. As expected, neither surface oxide shows affinity toward further O addition. However, we observed a significant difference in the interaction of SO₃ with the oxidized surfaces. The molecular binding energy of SO₃ on Pd vs Pt surface oxide layers was −0.91 and −0.12 eV, respectively, that is, SO₃ prefers to adsorb on PdO than on PtO₂. This large difference indicates that such interaction is a key descriptor and a prerequisite for the higher sulfation tendency of Pd than Pt. As expected, our results showed that the coadsorption SO₃ *and* O was not favored by both oxidized surfaces, due to the unwelcoming nature of the oxidized metal surface toward additional oxygen. Further details are given in Supporting Information.

Interaction of SO₃ and oxidized metal surface could lead to the formation of a surface sulfate layer and ultimately to the bulk sulfate phase. Unlike surface oxide phases of Pt and Pd, we do not have experimental information about the structure/morphology of the surface sulfate phases. Hence, we utilized the structural information on bulk sulfates to create surface
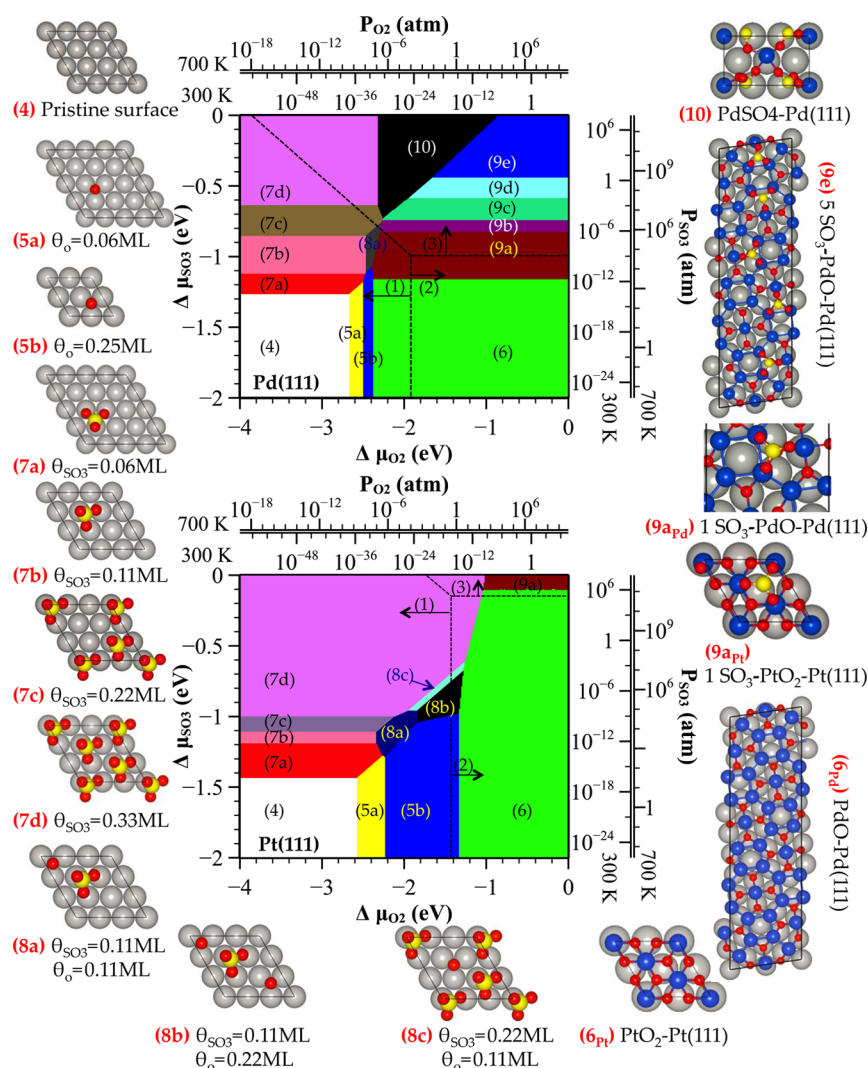
Figure 5. Surface phase diagrams of Pd(111) (top panel) and Pt(111) (bottom panel) surfaces in a constrained thermodynamic equilibrium with SO_3 and O_2. The given chemical potential range of oxygen ($\Delta\mu_{O_2}$) and SO_3 ($\Delta\mu_{SO_3}$) are translated into a pressure range for two representative temperatures (300 and 700 K). The numbering of the phases in each panel and structural models is adapted according to Figure 1. Common structural models for both Pt and Pd phases are represented by a single structure and corresponding structural number, whereas the different structural models of the same phase of Pt and Pd are subscripted (Pt or Pd) in the panel number (e.g., structures 6 and 9a). Structural models for 9b, 9c, and 9d of the top panel are not shown here for brevity, whereas the final structure 9e is shown. Dotted lines represent the bulk phase boundaries. Bulk phases numbering are shown with black arrows showing the respective regions. Bulk structural models are not shown here. Silver, red, and yellow spheres represent the Pt or Pd, oxygen, and sulfur, respectively. Blue spheres represent the Pt or Pd in the surface oxide or surface sulfate models.

sulfate models for both Pt and Pd. From the known structure of $PdSO_4$ and the predicted most stable structure of $PtSO_4$, we created a sulfate layer and placed this on the $(3 \times \sqrt{3})$ surface supercell of the (111) surface of Pt or Pd to minimize the lattice strain. The choice of this surface supercell was the best possible compromise considering the size and computational cost restrictions. The structural model of the Pd surface sulfate is shown in panel 10 of Figure 5. Further details and other models are provided in the Supporting Information.

Assembling the information about the entire spectrum of stable phases discussed above, we have constructed phase diagrams for oxidizing and sulfating conditions on Pd(111) and Pt(111) surfaces as shown in Figure 5. Because the entropic contribution to free energy due to vibrations is negligible and only temperature dependent, we have neglected the contribution to construct the phase diagrams. In this work, the inclusion

of vibrational contributions does not alter the outcome of the phase diagram, as the relative magnitude is <25 meV/Å^2 for the practically relevant temperature range of below 700 K. The impact of including the maximum vibrational contributions results in rather minor changes (up to 0.07 eV shift in O adsorbed phase boundaries and up to 0.16 eV shift in SO_3 adsorbed phase boundaries) to the features of the phase diagrams (most notably, a small shift in the phase boundaries in the phases with SO_3 adsorption). For example, at 300 K, the change of $\Delta\mu_{O_2}$ from −2.64 to −2.59 eV corresponds to an incredibly small pressure change of about −2.2 × 10^{-36} atm. Hence, none of the new stable structures disappears (or appears) from (or into) the phase diagram. Although this analysis provides a justification for neglecting the vibrational contribution in many prior studies,[15,30] we note that the inclusion of such contributions may be useful for complex
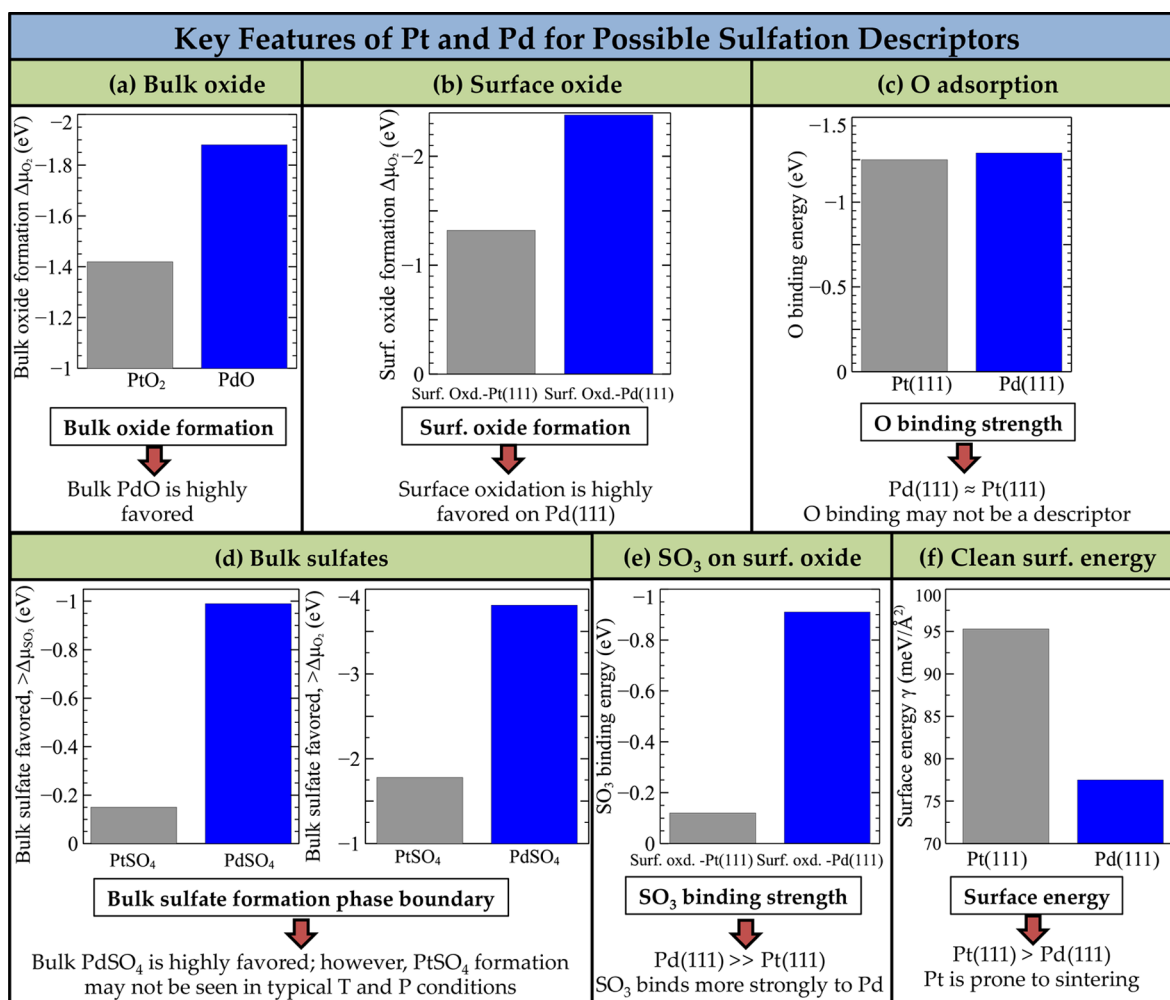
Figure 6. Key descriptors for metal oxidation and sulfation. Panel a: $\Delta\mu_{O_2}$ onset point for bulk oxide formation. Panel b: $\Delta\mu_{O_2}$ onset point for surface oxide formation. Panel c: oxygen binding energy on the pristine (111) surfaces. Panel d: bulk sulfate phase boundary onset point on $\Delta\mu_{O_2}$ and $\Delta\mu_{SO_3}$ scales. Panel e: SO_3 binding strength on the surface oxides. Panel f: surface energy of pristine (111) surfaces. Significant differences are seen between Pt and Pd for all features, except in case of panel c (O binding energy).

systems. The computed vibrational contributions for various adsorbed phases are shown in Figures S6 and S7 in the Supporting Information.

The surface phase diagram, as portrayed in Figure 5, is fairly complex due to possible existence of many phases. The chemical potentials of O_2 and SO_3 (using $\Delta\mu_{O_2}$ and $\Delta\mu_{SO_3}$) represent the x and y axes, respectively. Two more intuitive pressure scales (at representative temperatures of 300 and 700 K) are shown opposite to the chemical potential range. Starting from the lower left corner of the phase diagram (i.e., low chemical potential region of O_2 and SO_3), we observe a stable clean metal surface phase in both cases (Pd and Pt). We clearly see a tendency to get oxidized easily in the case of Pd surface due to the oxygen chemical potential demarcation ($\Delta\mu_{O_2} = -2.52$ eV for Pd and $\Delta\mu_{O_2} = -2.21$ eV for Pt in the case of experimentally known $p(2 \times 2)$ phase) favoring the O adsorption (panel 5b of Figure 5). While keeping the SO_3 concentration low and moving toward higher O_2 chemical potential (horizontal direction), we encounter an experimentally observed stable phase of $p(2 \times 2)$-O overlayer[38] (i.e., $\theta_O = 0.25$ ML, panel 5b of Figure 5) on both surfaces after the low coverage phase of $\theta_O = 0.06$ ML. We note that the

experimentally observed $c(2 \times 2)$-O overlayer (i.e., $\theta_O = 0.5$ ML) − most likely a metastable phase before transforming to a more stable surface oxide phase−was not identified as a stable phase in our study. Furthermore, the kinetics will also play a role[30] for the transformation of the $c(2 \times 2)$-O overlayer structure to the surface oxide phase. A further increase in O_2 chemical potential leads to the formation of stable surface oxide phases (panel 6 of Figure 5) on both surfaces. Besides the experimentally observed morphological differences, these two phases deeply contrast in oxidation affinity. The onset of surface oxide formation on Pd(111) surface is from $\Delta\mu_{O_2} = -2.38$ eV, whereas the onset point for the same on Pt(111) surface is from $\Delta\mu_{O_2} = -1.32$ eV. As seen experimentally,[6] our results suggest that the oxidized phase of Pd, unlike the more stable metallic state of Pt, is the most prevalent state in relevant catalytic conditions ($P \sim 1$ atm and $T \sim 200-500$ °C).

Moving toward higher SO_3 chemical potential region while keeping the O_2 chemical potential low (vertical direction), we observed multiple stable phases of SO_3 (represented by a range of $\theta_{SO_3} = 0.11-0.33$ ML, panels 7a−d of Figure 5) on both metal surfaces. Further increase in coverage of SO_3 on the metal surface is not stable due to the bulky nature of the

molecule, and it falls beyond the realistic temperature and pressure ranges. Stronger binding strength of SO_3 with Pt (111) translates to the higher coverage favorability of SO_3 on Pt(111) than on Pd(111) surface ($\Delta\mu_{SO_3}$ = −0.64 eV for Pd and −1.0 eV for Pt in the case of θ_{SO_3} = 0.33 ML).

Toward the higher chemical potential region along the diagonal (i.e., higher chemical potential for both O_2 and SO_3), we observed quite different behaviors on both metal surfaces. Unlike a single coadsorbed phase in case of Pd (panel 8a of Figure 5), multiple such phases were stable on the Pt surface (panels 8a−c of Figure 5). We observed a stable phase of SO_3 on the surface oxide of Pd (panels 9a−e of Figure 5), but this feature was absent in the case of Pt surface oxide at practically relevant temperature and pressure conditions (the phase boundary starts at $\Delta\mu_{SO_3}$ = −1.15 eV for Pd and −0.1 eV for Pt). This result aligns well with the idea of a prerequisite state to proceed toward the surface sulfate and ultimately the bulk metal sulfate of Pd. We note that the surface sulfate phase (panel 10 of Figure 5) for Pd(111) appears at a reasonably low chemical potential, which agrees with the experimental observation of $PdSO_4$ formation under typical operating conditions. In the case of Pt, surface sulfate phase does not appear to be a stable phase. In realistic temperature and pressure conditions, we expect to have coadsorbed phases of O and SO_3, surface-oxide phases of Pd, surface sulfate phase of Pd, and eventually the bulk sulfate phase of Pd.

On the basis of the observations so far, we briefly discuss the key insights and outcomes of this study. Figure 6 shows a comparison of the key features of the Pd(111) and Pt(111) surfaces. (a) Panel a shows the O_2 chemical potential difference in bulk oxide formation. Clearly, PdO formation is preferred over PtO_2 even at low oxygen chemical potential. (b) Panel b compares the O_2 chemical potential for surface oxide formation. We observe that the surface oxide formation is favored on Pd than Pt. (c) Panel c shows a rather indistinguishable O binding strength on both surfaces. This behavior aligns well with our natural belief of both metals being rather similar due to other physical/morphological properties such as metal−oxygen bond length (∼2 Å), most stable adsorption sites (3-fold *fcc*), nature of charge transfer between metal−oxygen during adsorption[37] (d) On the other hand, the sulfation behavior is quite different for the two metals. Panel d compares the phase boundary onset of bulk sulfate formation in terms of O_2 and SO_3 chemical potentials (also see Figure 2). It is clearly observed that $PdSO_4$ formation is highly favored, unlike $PtSO_4$, under typical operating conditions. (e) Panel e displays the significant difference in SO_3 binding strength on both surface oxide layers. SO_3 binds more strongly to PdO than PtO_2. (f) Panel f shows the surface energy comparison of pristine Pt(111) and Pd(111) surfaces. As observed experimentally,[39,40] lower surface energy of Pd compared to Pt is associated with the higher stability against sintering. This explains, along with the cost factor, why modern DOCs are bimetallic (Pt/Pd) in nature. Except for oxygen binding, all other key features can serve as descriptors for catalyst sulfation and the resulting deactivation, and hence we believe that they can be utilized for faster and effective screening of the potential sulfur resistant catalysts.

We note that a few assumptions have been made in our work. First, our choice of surface plane is the (111) facet of Pt and Pd. Even though the catalyst nanoparticles contain many types of facets due to polycrystalline nature, the (111) facet is known to be the dominant, most stable, and one of the most active

surfaces.[41,42] Second, we do not consider metal−support interactions in this study. The support can have a significant influence in some catalytic systems; however the Al_2O_3 support, typically used in emissions oxidation catalysts, is relatively inert.[43] Hence, we do not expect the support to impact or alter the main conclusions of this work. Third, we have constructed the surface sulfate model by placing bulk sulfate on the metal surface. Nevertheless, we believe our model captures the essence of a surface sulfate phase. Fourth, accuracy of the results presented here will depend on the choice of functional. However, given the number of cases considered and the sizes of systems for each case, considering nonlocal exchange-correlation functionals (e.g., hybrid functionals) would be computational-cost prohibitive. Furthermore, we found that the PBE functional is also adequate to address the structure of van der Waals bonded PtO_2 layers. We calculated the energetics of the PtO_2−Pt(111) system with van der Waals interactions using the DFT-D2 functional[44] The difference in total energy was <2.2 meV/atom when van der Waals interactions were included. Thus, only the PBE functional was used throughout, and all conclusions were consistently reached using this functional. It is expected that the qualitative aspects of our results and our main conclusions will not be impacted by the usage of a higher level functional. Finally, we have only considered the thermodynamic aspects in this study. Although kinetics also plays an important role during phase transformations, the stability and possibility of the formation of such phases is controlled by thermodynamics and should be considered first, before kinetic aspects are explored.

In summary, we have investigated the bulk and surface sulfation phenomena of Pt and Pd under catalytically relevant temperature and pressure conditions using first-principles thermodynamics. Bulk and surface phase diagrams were constructed and possible stable phases en route to sulfation were identified. The bulk phase diagrams clearly suggested that the oxidation and sulfation of Pd is highly favored whereas metallic form of Pt is favored under catalytically relevant conditions. The surface phase diagrams clearly showed some remarkable differences between Pt (111) and Pd(111) surfaces in oxidizing and sulfating environments. Our results showed that the oxidized metal surfaces (i.e., surface oxides) are the key to understand sulfation. Pd showed a great affinity to form the surface oxide phase and showed significant SO_3-to-surface oxide binding strength. On the other hand, surface oxide layer formation is relatively less favored and SO_3-to-surface oxide binding strength was significantly smaller for Pt. Furthermore, the surface sulfate phase formation was favored only on Pd(111) in catalytically relevant conditions. The aforementioned key features can be used to screen materials to identify potential candidates for sulfur resistant catalysts.

■ COMPUTATIONAL METHODS

Our first-principles calculations were carried out using density functional theory (DFT)[45,46] as implemented in the VASP code[47] with the electronic wave functions expanded in a plane wave basis with a cutoff energy of 400 eV. All calculations were performed utilizing the Perdew−Burke−Ernzerhof (PBE) functional,[48] the projector augmented wave (PAW) frozen-core potentials, and spin polarization method. The structures were relaxed using a conjugate-gradient algorithm until the forces on all atoms were <0.01 eV/Å. Both the Pt(111) and Pd(111) surfaces were represented by a five-layer slab, and (2 × 2), (3 × 3), and (4 × 4) surface unit cells. Two bottom layers

of the slab were fixed and the remaining top three layers were allowed to relax. To avoid any interactions between periodic images, a 12−14 Å thick vacuum region was introduced. Monkhorst−Pack grids of $3 \times 3 \times 1$, $4 \times 4 \times 1$, and $5 \times 5 \times 1$ were used for Brillouin zone integration for slabs with (4×4), (3×3), and (2×2) surface unit cells, respectively. For the Pt surface-oxide models, PtO_2−Pt(111) and Pd surface oxides, PdO−Pd(111), Monkhorst−Pack grids of $5 \times 5 \times 1$ and $1 \times 3 \times 1$ were used, respectively. Similarly, a Monkhorst−Pack grid of $4 \times 5 \times 1$ was used for both Pt and Pd surface-sulfate models with $(3 \times \sqrt{3})$ supercell. To search the possible $PtSO_4$ structures, evolutionary structure prediction was performed using the USPEX code[13,14] in conjunction with ab initio structure relaxations using DFT and methodology as mentioned above.

ASSOCIATED CONTENT

S Supporting Information

Further details on evaluation of surface and bulk free energy from the first-principles thermodynamics, computation of vibrational contributions to the free energy, various bulk parameters, evolutionary algorithm based structure prediction, oxygen adsorption on Pt and Pd surfaces, adsorption of SO_3 on both metal surfaces, coadsorptions of oxygen and SO_3, estimation of cross-interaction during adsorption of oxygen and SO_3, adsorption on surface oxides, surface sulfate models, and the vibrational contributions to the free energy are provided. This material is available free of charge via the Internet at http://pubs.acs.org.

AUTHOR INFORMATION

Corresponding Author
*E-mail: rampi@ims.uconn.edu.

Present Address
†ExxonMobil Research and Engineering, Annandale, NJ 08801, United States.

Notes
The authors declare no competing financial interest.

ACKNOWLEDGMENTS

REFERENCES

(1) Summers, J. C. Reaction of Sulfur Oxides with Alumina and Platinum/Alumina. *Environ. Sci. Technol.* **1979**, *13*, 321−325.

(2) Taylor, K. C. Sulfur Storage on Automotive Catalysts. *Product R&D* **1976**, *15*, 264−268.

(3) Kröcher, O.; Widmer, M.; Elsener, M.; Rothe, D. Adsorption and Desorption of SO_x on Diesel Oxidation Catalysts. *Ind. Eng. Chem. Res.* **2009**, *48*, 9847−9857.

(4) Mowery, D. L.; Graboski, M. S.; Ohno, T. R.; McCormick, R. L. Deactivation of PdO−Al_2O_3 Oxidation Catalyst in Lean-Burn Natural Gas Engine Exhaust: Aged Catalyst Characterization and Studies of Poisoning by H_2O and SO_2. *Appl. Catal., B* **1999**, *21*, 157−169.

(5) Bartholomew, C. H. Mechanisms of Catalyst Deactivation. *Appl. Catal., A* **2001**, *212*, 17−60.

(6) Sharma, H. N.; Suib, S. L.; Mhadeshwar, A. B. Interactions of Sulfur Oxides With Diesel Oxidation Catalysts (DOCs). In *Novel Materials for Catalysis and Fuels Processing*; Oxford University Press: New York, 2013; Vol. *1132*, pp 117−155.

(7) Russell, A.; Epling, W. S. Diesel Oxidation Catalysts. *Catal. Rev. Sci. Eng.* **2011**, *53*, 337−423.

(8) Mowery, D. L.; McCormick, R. L. Deactivation of Alumina Supported and Unsupported PdO Methane Oxidation Catalyst: the Effect of Water on Sulfate Poisoning. *Appl. Catal., B* **2001**, *34*, 287−297.

(9) Truex, T. Interaction of Sulfur with Automotive Catalysts and the Impact on Vehicle Emissions-A Review. *SAE Tech. Pap.* **1999**, 1999-01-1543.

(10) Corro, G. Sulfur Impact on Diesel Emission Control- A Review. *React. Kinet. Catal. Lett.* **2002**, *75*, 89−106.

(11) McAllister, B.; Hu, P. A Density Functional Theory Study of Sulfur Poisoning. *J. Chem. Phys.* **2005**, *122*, 084709−084715.

(12) Happel, M.; Luckas, N.; Viñes, F.; Sobota, M.; Laurin, M.; Görling, A.; Libuda, J. SO_2 Adsorption on Pt(111) and Oxygen Precovered Pt(111): A Combined Infrared Reflection Absorption Spectroscopy and Density Functional Study. *J. Phys. Chem. C* **2011**, *115*, 479−491.

(13) Oganov, A. R.; Glass, C. W. Crystal Structure Prediction Using Ab Initio Evolutionary Techniques: Principles and Applications. *J. Chem. Phys.* **2006**, *124*, 244704−244719.

(14) Glass, C. W.; Oganov, A. R.; Hansen, N. USPEX—Evolutionary Crystal Structure Prediction. *Comput. Phys. Commun.* **2006**, *175*, 713−720.

(15) Zhu, H.; Tang, C.; Ramprasad, R. Phase Equilibria at Si-HfO_2 and Pt-HfO_2 Interfaces from First Principles Thermodynamics. *Phys. Rev. B* **2010**, *82*, 235413.

(16) Dianat, A.; Seriani, N.; Bobeth, M.; Pompe, W.; Ciacchi, L. C. DFT Study of the Thermodynamic Stability of Pd−Pt Bulk Oxide Phases. *J. Phys. Chem. C* **2008**, *112*, 13623−13628.

(17) Sharma, H. N.; Sharma, V.; Huan, T. D. Exploring $PtSO_4$ and $PdSO_4$ Phases: An Evolutionary Algorithm Based Investigation. **2015**, http://arxiv.org/abs/1503.02752.

(18) Parker, D. H.; Bartram, M. E.; Koel, B. E. Study of High Coverages of Atomic Oxygen on the Pt(111) Surface. *Surf. Sci.* **1989**, *217*, 489−510.

(19) Saliba, N. A.; Tsai, Y. L.; Panja, C.; Koel, B. E. Oxidation of Pt(111) by Ozone (O_3) Under UHV Conditions. *Surf. Sci.* **1999**, *419*, 79−88.

(20) Krasnikov, S. A.; Murphy, S.; Berdunov, N.; McCoy, A. P.; Radican, K.; Shvets, I. V. Self-limited Growth of Triangular PtO_2 Nanoclusters on the Pt(111) Surface. *Nanotechnology* **2010**, *21*, 335301.

(21) Gabasch, H.; Unterberger, W.; Hayek, K.; Klötzer, B.; Kresse, G.; Klein, C.; Schmid, M.; Varga, P. Growth and Decay of the Pd(111)−Pd_5O_4 Surface Oxide: Pressure-Dependent Kinetics and Structural Aspects. *Surf. Sci.* **2006**, *600*, 205−218.

(22) Zemlyanov, D.; Aszalos-Kiss, B.; Kleimenov, E.; Teschner, D.; Zafeiratos, S.; Hävecker, M.; Knop-Gericke, A.; Schlögl, R.; Gabasch, H.; Unterberger, W.; et al. In Situ XPS Study of Pd(111) Oxidation. Part 1:2D Oxide Formation in 10^{-3} mbar O_2. *Surf. Sci.* **2006**, *600*, 983−994.

(23) Diebold, U.; Li, S.; Schmid, M. Oxide Surface Science. *Annu. Rev. Phys. Chem.* **2010**, *61*, 129−148.

(24) Klikovits, J.; Napetschnig, E.; Schmid, M.; Seriani, N.; Dubay, O.; Kresse, G.; Varga, P. Surface Oxides on Pd(111): STM and Density Functional Calculations. *Phys. Rev. B* **2007**, *76*, 045405.

(25) Devarajan, S. P.; Hinojosa, J. A., Jr.; Weaver, J. F. STM Study of High-Coverage Structures of Atomic Oxygen on Pt(111): p(2 × 1) and Pt Oxide Chain Structures. *Surf. Sci.* **2008**, *602*, 3116−3124.

(26) Lundgren, E.; Mikkelsen, A.; Andersen, J.; Kresse, G.; Schmid, M.; Varga, P. Surface oxides on close-packed surfaces of late transition metals. *J. Phys.: Condens. Matter* **2006**, *18*, R481−R499.

(27) Todorova, M.; Reuter, K.; Scheffler, M. Oxygen Overlayers on Pd(111) Studied by Density Functional Theory. *J. Phys. Chem. B* **2004**, *108*, 14477−14483.

(28) Todorova, M.; Li, W. X.; Ganduglia-Pirovano, M.; Stampfl, C.; Reuter, K.; Scheffler, M. Role of Subsurface Oxygen in Oxide Formation at Transition Metal Surfaces. *Phys. Rev. Lett.* **2002**, *89*, 096103.

(29) Todorova, M.; Reuter, K.; Scheffler, M. Density-Functional Theory Study of the Initial Oxygen Incorporation in Pd(111). *Phys. Rev. B* **2005**, *71*, 195403.

(30) Rogal, J.; Reuter, K.; Scheffler, M. CO Oxidation at Pd(100): A First-Principles Constrained Thermodynamics Study. *Phys. Rev. B* **2007**, *75*, 205433.

(31) Voogt, E. H.; Mens, A. J. M.; Gijzeman, O. L. J.; Geus, J. W. Adsorption of Oxygen and Surface Oxide Formation on Pd(111) and Pd Foil Studied with Ellipsometry, LEED, AES and XPS. *Surf. Sci.* **1997**, *373*, 210−220.

(32) Kan, H. H.; Weaver, J. F. A PdO(1 0 1) Thin Film Grown on Pd(111) in Ultrahigh Vacuum. *Surf. Sci.* **2008**, *602*, L53−L57.

(33) Engström, U.; Ryberg, R. Atomic Oxygen on a Pt(111) Surface Studied by Infrared Spectroscopy. *Phys. Rev. Lett.* **1999**, *82*, 2741−2744.

(34) Campbell, C. T.; Ertl, G.; Kuipers, H.; Segner, J. A Molecular Beam Study of the Adsorption and Desorption of Oxygen From a Pt(111) Surface. *Surf. Sci.* **1981**, *107*, 220−236.

(35) Ackermann, M. D. PhD Thesis, Operando SXRD: a New View on Catalysis, Leiden University, 2007.

(36) Leisenberger, F. P.; Koller, G.; Sock, M.; Surnev, S.; Ramsey, M. G.; Netzer, F. P.; Klötzer, B.; Hayek, K. Surface and Subsurface Oxygen on Pd(111). *Surf. Sci.* **2000**, *445*, 380−393.

(37) Sharma, H. N.; Sharma, V.; Hamzehlouyan, T.; Epling, W.; Mhadeshwar, A. B.; Ramprasad, R. SO$_x$ Oxidation Kinetics on Pt(111) and Pd(111): First Principles Computations Meet Microkinetic Modeling. *J. Phys. Chem. C* **2014**, *118*, 6934−6940.

(38) Gland, J. L. Molecular and Atomic Adsorption of Oxygen on the Pt(111) and Pt(S)-12(111) × (111) Surfaces. *Surf. Sci.* **1980**, *93*, 487−514.

(39) Spivey, J. J.; Butt, J. B. Literature Review: Deactivation of Catalysts in the Oxidation of Volatile Organic Compounds. *Catal. Today* **1992**, *11*, 465−500.

(40) Hegedus, L. L.; Summers, J. C.; Schlatter, J. C.; Baron, K. Poison-Resistant Catalysts for the Simultaneous Control of Hydrocarbon, Carbon Monoxide, and Nitrogen Oxide Emissions. *J. Catal.* **1979**, *56*, 321−335.

(41) Solla-Gullon, J.; Vidal-Iglesias, F. J.; Feliu, J. M. Shape Dependent Electrocatalysis. *Annu. Rep. Prog. Chem., Sect. C: Phys. Chem.* **2011**, *107*, 263−297.

(42) Gómez-Marín, A. M.; Rizo, R.; Feliu, J. M. Some Reflections on the Understanding of the Oxygen Reduction Reaction at Pt(111). *Beilstein J. Nanotechnol.* **2013**, *4*, 956−967.

(43) Sharma, H. N.; Mhadeshwar, A. B. A Detailed Microkinetic Model for Diesel Engine Emissions Oxidation on Platinum Based Diesel Oxidation Catalysts (DOC). *Appl. Catal., B* **2012**, *127*, 190−204.

(44) Grimme, S. Semiempirical GGA-Type Density Functional Constructed with a Long-Range Dispersion Correction. *J. Comput. Chem.* **2006**, *27*, 1787−1799.

(45) Hohenberg, P.; Kohn, W. Inhomogeneous Electron Gas. *Phys. Rev.* **1964**, *136*, B864−B871.

(46) Kohn, W.; Sham, L. J. Self-Consistent Equations Including Exchange and Correlation Effects. *Phys. Rev.* **1965**, *140*, A1133−A1138.

(47) Kresse, G.; Furthmüller, J. Efficiency of Ab-Initio Total Energy Calculations for Metals and Semiconductors Using a Plane-Wave Basis Set. *Comput. Mater. Sci.* **1996**, *6*, 15−50.

(48) Perdew, J. P.; Burke, K.; Ernzerhof, M. Generalized Gradient Approximation Made Simple. *Phys. Rev. Lett.* **1996**, *77*, 3865−3868.